The Astronomical Journal, 170:203 (14pp), 2025 October
https://doi.org/10.3847/1538-3881/adf6db

Searching for GEMS: TOI-7149 b, an Inflated Giant Planet Causing a 12% Transit of a Fully Convective M-dwarf

Shubham Kanodia[1], Caleb I. Cañas[2,20], Suvrath Mahadevan[3,4], Andrea S.J. Lin[5], Henry A. Kobulnicky[6], Ian Karfs[6], Alexina Birkholz[6], Andrew Monson[7], Arvind F. Gupta[8], Mark Everett[8], Michael Rodruck[9], Rowen I. Glusman[10], Te Han[11], William D. Cochran[12,13], Chad F. Bender[7], Scott A. Diddams[14,15], Daniel Krolikowski[7], Samuel Halverson[16], Jessica Libby-Roberts[3,4], Joe P. Ninan[17], Paul Robertson[11], Arpita Roy[18], Christian Schwab[19], and Guđmundur Stefánsson[10]

[1] Carnegie Science Earth and Planets Laboratory, 5241 Broad Branch Road, NW, Washington, DC 20015, USA; skanodia@carnegiescience.edu
[2] NASA Goddard Space Flight Center, 8800 Greenbelt Road, Greenbelt, MD 20771, USA
[3] Department of Astronomy & Astrophysics, 525 Davey Laboratory, The Pennsylvania State University, University Park, PA 16802, USA
[4] Center for Exoplanets and Habitable Worlds, 525 Davey Laboratory, The Pennsylvania State University, University Park, PA 16802, USA
[5] Department of Astronomy, California Institute of Technology, 1200 East California Boulevard, Pasadena, CA 91125, USA
[6] Department of Physics & Astronomy, University of Wyoming, Laramie, WY 82070, USA
[7] Steward Observatory, The University of Arizona, 933 North Cherry Avenue, Tucson, AZ 85721, USA
[8] U.S. National Science Foundation National Optical-Infrared Astronomy Research Laboratory, 950 North Cherry Avenue, Tucson, AZ 85719, USA
[9] Department of Physics, Engineering, and Astrophysics, Randolph-Macon College, Ashland, VA 23005, USA
[10] Anton Pannekoek Institute for Astronomy, University of Amsterdam, Science Park 904, 1098 XH Amsterdam, The Netherlands
[11] Department of Physics & Astronomy, The University of California, Irvine, CA 92697, USA
[12] McDonald Observatory and Department of Astronomy, The University of Texas at Austin, USA
[13] Center for Planetary Systems Habitability, The University of Texas at Austin, USA
[14] Electrical, Computer & Energy Engineering, University of Colorado, 1111 Engineering Drive, Boulder, CO 80309, USA
[15] Department of Physics, University of Colorado, 2000 Colorado Avenue, Boulder, CO 80309, USA
[16] Jet Propulsion Laboratory, California Institute of Technology, 4800 Oak Grove Drive, Pasadena, CA 91109, USA
[17] Department of Astronomy and Astrophysics, Tata Institute of Fundamental Research, Homi Bhabha Road, Colaba, Mumbai 400005, India
[18] Astrophysics & Space Institute, Schmidt Sciences, New York, NY 10011, USA
[19] School of Mathematical and Physical Sciences, Macquarie University, Balaclava Road, North Ryde, NSW 2109, Australia

Received 2025 June 21; revised 2025 July 23; accepted 2025 July 28; published 2025 September 3

Abstract

We describe the discovery and characterization of TOI-7149 b, a 0.705 0.075 M_J, 1.18 0.045 R_J gas giant on a 2.65 days period orbit transiting an M4V star with a mass of 0.344 0.030 $M_\odot$ and an effective temperature of 3363 59 K. The planet was first discovered using NASA's TESS mission, which we confirmed using a combination of ground-based photometry, radial velocities, and speckle imaging. The planet has one of the deepest transits of all known main-sequence planet hosts at 12% ($R_p/R_\star$ 0.33). Pushing the bounds of previous discoveries of giant exoplanets around M-dwarf stars (GEMS), TOI-7149 is one of the lowest mass M-dwarfs to host a transiting giant planet. We compare the sample of transiting GEMS to stars within 200 pc with a Gaia color–magnitude diagram and find that the GEMS hosts are likely to be high metallicity stars. We also analyze the sample of transiting giant planets using the nonparametric `MRExo` framework to compare the bulk density of warm Jupiters across stellar masses. We confirm our previous result that transiting Jupiters around early M-dwarfs have similar masses and densities to warm Jupiters around FGK stars, and extend this to mid M-dwarfs, thereby suggesting a potential commonality in their formation mechanisms.

Unified Astronomy Thesaurus concepts: M dwarf stars (982); Extrasolar gaseous giant planets (509); Astrostatistics (1882); Radial velocity (1332)

1. Introduction

TESS's all sky coverage includes millions of bright nearby stars (G. R. Ricker et al. 2014), particularly M-dwarfs. These stars form the majority of the stars in the Galaxy (T. J. Henry et al. 2006; C. Reylé et al. 2021), and have been well-studied for their abundance of terrestrial planets, both from the transit technique with Kepler/K2 (C. D. Dressing & D. Charbonneau 2013; K. K. Hardegree-Ullman et al. 2019; D. C. Hsu et al. 2020, etc.) and radial velocities (RVs; X. Bonfils et al. 2013; S. Sabotta et al. 2021, etc.). However, the study of giant planets around M-dwarfs has historically been facilitated by minimum mass measurements of nontransiting RV detections (M. Endl et al. 2006; J. A. Johnson et al. 2010; X. Bonfils et al. 2013; J. Maldonado et al. 2019; S. Sabotta et al. 2021; M. Schlecker et al. 2022; E. K. Pass et al. 2023), the planetary natures of which are uncertain due to the sin *i* degeneracy. This has been changing recently due to detections of giant exoplanets around M-dwarf stars (GEMS) from TESS (e.g., C. I. Cañas et al. 2020; S. Kanodia et al. 2023c; M. J. Hobson et al. 2023; L. M. Bernabò et al. 2024; R. B. Fernandes et al. 2025) that have enabled statistical analysis of the bulk properties of these planets (S. Müller & R. Helled 2025; S. Kanodia 2024), their host-star metallicity dependence (T. Gan et al. 2025), their atmospheres (C. I. Cañas et al. 2025), and their occurrence rates (E. M. Bryant et al. 2023; T. Gan et al. 2023). However, this sample is still limited and, in particular, is biased toward early M-dwarf hosts. Thus, we

---

[20] NASA Postdoctoral Fellow

have started the Searching for GEMS survey (S. Kanodia et al. 2024a) to help mitigate this.

TIC-459323923.01 was identified as a planet candidate during development of our custom `TESS-miner Python` package (R. I. Glusman et al. 2025, in preparation), which was developed to identify transiting GEMS in a volume-limited 200 pc sample of 1 million M-dwarfs observed by TESS as part of the Searching for GEMS survey (S. Kanodia et al. 2024a). It was identified by our pipeline in 2024 May, after which we began ground-based observations. TIC-459323923.01 was subsequently identified as a TESS object of interest (TOI) 7149.01 by the Faint-star Search (M. Kunimoto et al. 2022) using the Quick Look Pipeline algorithm developed by C. X. Huang et al. (2020) in 2024 October. We adopt TOI-7149 as the host star name for this manuscript and discuss our observations in Section 2, which include TESS photometry as well as ground-based photometry from the Red Buttes Observatory (RBO), the 200 inch Hale Telescope at Palomar, and the Three-hundred Millimeter Telescope (TMMT), and Las Campanas Remote Observatory (LCRO) at Las Campanas. We then describe our spectroscopic follow-up using the Habitable-zone Planet Finder (HPF). In Section 3, we discuss the estimated stellar characteristics, and the procedure followed to fit the observations and obtain planetary parameters in Section 4. In Section 5, we contextualize TOI-7149 b in the landscape of other transiting GEMS, as well as discuss sample-level trends seen for transiting giant planets across the stellar mass axis, before summarizing our results and concluding in Section 6.

2. Observations

2.1. TESS

TESS observed TOI-7149 across five sectors (25, 51, 52, 78, 79) with a baseline spanning 4 yr. Sector 78 is excluded from further analysis due to excessive stray and background light contamination over the majority of the light curve. Of the remaining sectors, TOI-7149 was observed in Sector 25 in 2020 May with an 1800 s cadence, in Sectors 51–52 from 2022 May to June at 600 s cadence, and in Sector 79 in 2024 June with a 200 s cadence.

We extracted the light curves from the TESS full-frame images (FFIs) using the TESS-Gaia Light Curve (`tglc`[21]) pipeline (T. Han & T. D. Brandt 2023). `tglc` models the TESS point-spread function (PSF) along with Gaia astrometry to estimate and correct for contamination in TESS photometry from nearby stars.

The `tglc` photometry for Sectors 25, 51, and 52 was extracted as part of the light-curve extraction procedure for the survey (R. I. Glusman et al. 2025, in preparation), where we used a 150 × 150 pixel cutout to estimate the empirical PSF needed to correct background contamination. For Sector 79, we used a 91 × 91 pixel cutout. As part of this, we also perform a sigma-clip to the aperture flux from `tglc` and detrend the clipped time series using `wotan` (M. Hippke et al. 2019). We first employ a "cosine" kernel with a kernel length of 10 days using `wotan` to remove low-frequency structure from the light curve. We then run a box-least squares (G. Kovács et al. 2002) periodogram over a period range of 1.0–12.0 days, and mask out the identified transits, before running a second detrending with `wotan`, this time with a higher frequency kernel of 0.5 days. These double-detrended light curves detect the planetary transit with a period of 2.65 days, and are used for subsequent analysis and are shown in Figure 1.

The closest background star, TIC-459323925 (Gaia DR3 1200751810900167040), is 0.6 mag brighter in Gaia *G* band, 0.1 mag brighter in TESS *T* band, and 17 away from TOI-7149 (Figure 2). This background star causes considerable dilution in TESS photometry, which necessitates the use of the `tglc` reduction to correct dilution. This contamination is also evinced by the TIC contamination ratio (K. G. Stassun et al. 2019) of 0.37 on ExoFOP,[22] which should be 0 when there is no light from additional sources in the aperture. While we use `tglc` to obtain a first-order dilution correction, we constrain the dilution further using ground-based observations that spatially resolve the background stars.

2.2. Ground-based Photometric Observations

2.2.1. 0.6 m RBO

We observed three transits of TOI-7149 b with the 0.6 m telescope at the RBO in Wyoming, USA (D. H. Kasper et al. 2016) on 2024 August 2, 2025 February 22 and 2025 March 10. We used the Bessell I filter with no on-chip binning and exposure times of 240 s for all observations. The plate scale for RBO is $0\farcs56$ pixel^{-1}, with a science aperture radius of 4–5 pixels ($2\farcs2$–$2\farcs8$) across the three transits. The light curves are shown in Figure 3.

2.2.2. 0.3 m TMMT

We observed a transit on 2024 August 26 using the using the TMMT (A. J. Monson et al. 2017) at Las Campanas Observatory in Chile. We used the Bessell I filter, without any on-chip binning, and used an exposure time of 180 s. The plate scale during these observations was $0\farcs97$ pixel^{-1}, and the science aperture radius was $4\farcs8$. The light curve is shown in Figure 3.

2.2.3. 0.3 m LCRO

We also used the 0.3 m LCRO telescope at the Las Campanas Observatory in Chile alongside TMMT on 2024 August 26. The data was taken unbinned, with a plate scale of $0\farcs64$ per pixel in SDSS *i'* band, and reduced with a science aperture radius of $2\farcs9$. The light curve is shown in Figure 3.

Data for RBO, TMMT, and LCRO were reduced with aperture photometry using the custom `Python` pipeline described in S. Kanodia et al. (2024b).

2.2.4. Diffuser-assisted 5.1 m Palomar Wide Field Infrared Camera

We observed a transit of TOI-7149 b in *J*-band ($\lambda_{\rm cent} = 1.25\,\mu$m) with the Wide Field Infrared Camera (J. C. Wilson et al. 2003) on the 5.1 m Hale telescope at Palomar Observatory in California, USA on 2025 May 18. The observations included an engineered diffuser to defocus the PSF (3 FWHM), which allowed for longer exposure times and increased photometric stability (G. Stefansson et al. 2017). The data cadence was 37 s, with 30 s exposures and 6–7 s for readout and processing. It was taken unbinned with a plate scale of $0\farcs249$ pixel^{-1}, and was reduced using `AstroImageJ` (K. A. Collins et al. 2017) with a science aperture radius of 19 pixels. The light curves are shown in Figure 3.

---

[21] https://github.com/TeHanHunter/TESS_Gaia_Light_Curve

[22] https://exofop.ipac.caltech.edu/tess/target.php?id=459323923

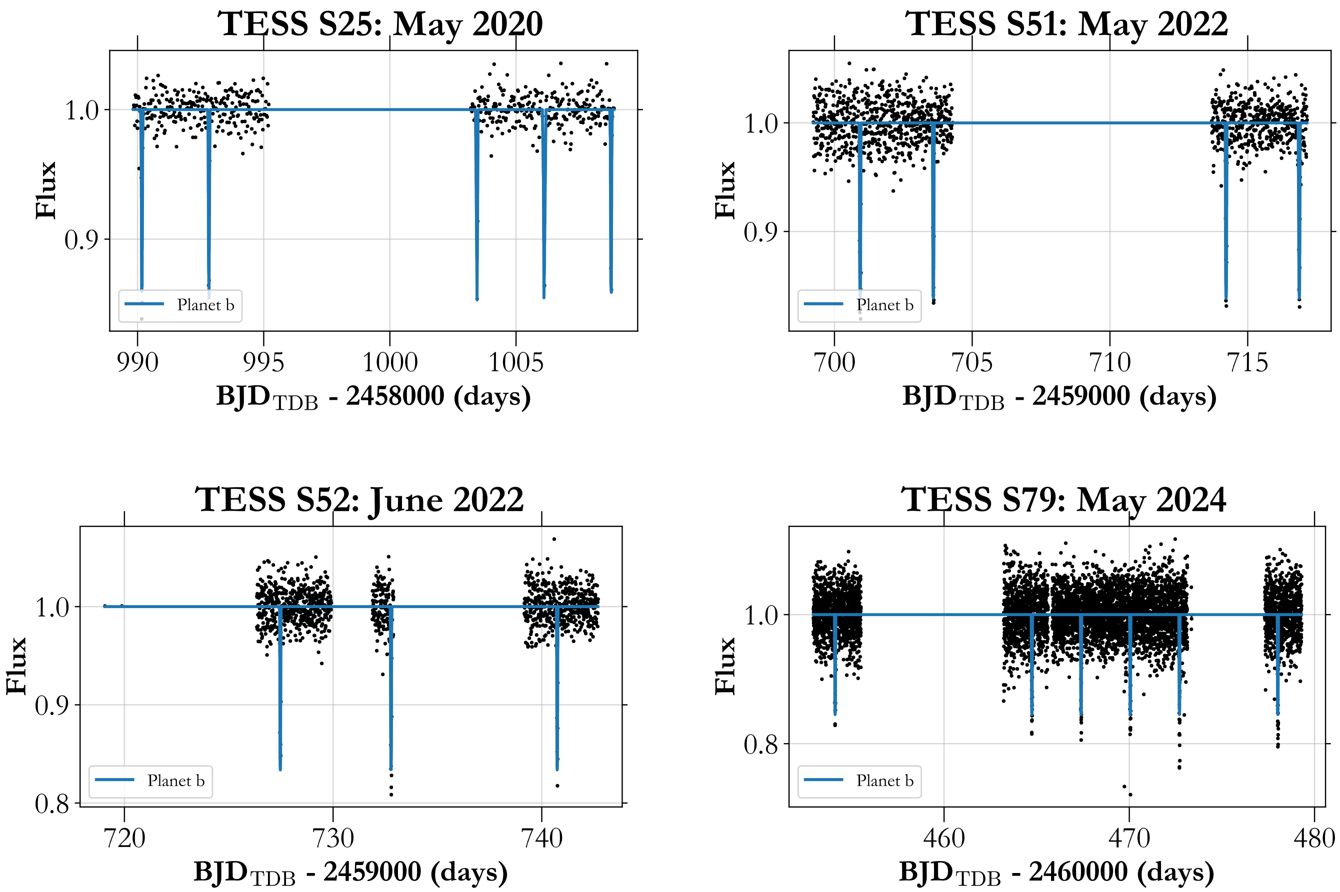

Figure 1. TESS photometry across sectors 25, 51, 52, and 79, with the best-fit model shown in blue.

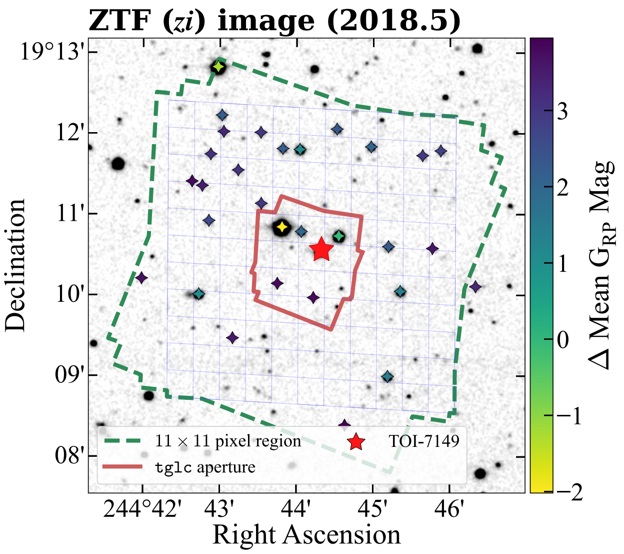

Figure 2. Overlaying the `tglc` 3 × 3 pixel aperture for all sectors (red) on a 11 × 11 TESS pixel footprint for all sectors. The blue grid is the 11 × 11 footprint for Sector 79. TOI-7149 is shown as a red star. Stars with $|\Delta G_{\rm RP}| < 4$ contained in the footprint are colored by their $\Delta G_{\rm RP}$ mag, showing the crowded field. The background image is from ZTF *zi* around 2018.5 (F. J. Masci et al. 2019).

2.3. High Contrast Imaging

We observed TOI-7149 using the NN-Explore Exoplanet Stellar Speckle Imager (NESSI; N. J. Scott et al. 2018) on the WIYN 3.5 m telescope located at Kitt Peak National Observatory on the nights of 2024 September 10, 2025 February 18, and 2025 February 19 (2024B-103024, 2025A-103024: PI Kanodia). Sequences of 40 ms diffraction-limited frames were collected in the SDSS *r*’ and *z*’ filters using the blue and red NESSI cameras, respectively. The individual frames were combined to produce reconstructed speckle images following the methods of S. B. Howell et al. (2011). We determined that image quality of the 2025 February 18 observation was higher than on the other nights, which were affected by poor observing conditions, so we elect to use this night for the remainder of our analysis. The speckle images and 5σ contrast limits are shown in Figure 4. We are able to exclude companions and background sources down to contrast limits of $\Delta m_{r'} = 4.4$ and $\Delta m_{z'} = 4.1$ at $0\farcs3$ and $\Delta m_{r'} = 4.7$ and $\Delta m_{z'} = 4.6$ at $1\farcs0$, confirming that the ground-based observations do not have additional sources of dilution.

2.4. Near-infrared Spectroscopy with HPF

We obtained 25 visits on TOI-7149 b using HPF (S. Mahadevan et al. 2012, 2014) between 2024 May 28 and 2025 March 29, which are shown in Figure 5. HPF is a near-infrared (8080–12780 Å) spectrograph on the 10 m Hobby–Eberly Telescope[23] (HET; L. W. Ramsey et al. 1998; G. J. Hill et al. 2021) in West Texas, USA. It is

---

[23] Based on observations obtained with the HET, which is a joint project of the University of Texas at Austin, the Pennsylvania State University, Ludwig-Maximillians-Universitaet Muenchen, and Georg-August Universitaet Goettingen. The HET is named in honor of its principal benefactors, William P. Hobby and Robert E. Eberly.

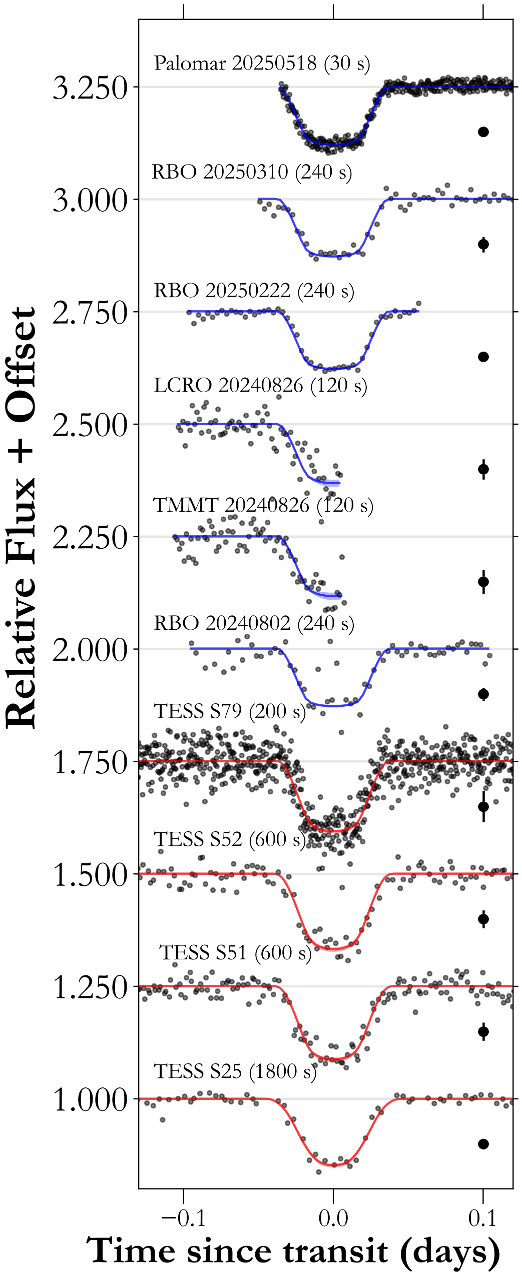

Figure 3. Photometric observations for TOI-7149 b phase-folded to the best-fit orbital period; each data set is separated by 0.25. The black points show the detrended data, while the model is shown as a solid, colored line along with the 1σ confidence intervals as translucent bands. We include the representative median statistical uncertainty at $x = 0.1$. Ground-based observations are used to measure the transit depth and ephemeris. The TESS data set (red models) is used to refine the ephemeris, with a floating dilution term, which is constrained using the ground-based photometry (blue models).

environmentally stabilized (G. Stefansson et al. 2016) and has fiber-fed illumination (S. Kanodia et al. 2018, 2021). We corrected for bias, nonlinearity, cosmic rays, and processed the HPF slope images using the `HxRGproc` package (J. P. Ninan et al. 2018). Given the faintness of the star and to avoid stray light contamination, we do not use the simultaneous calibration using the near-infrared laser frequency comb (LFC; A. J. Metcalf et al. 2019). Instead, we interpolated the wavelength solution from other LFC exposures on the night of the observation, which has been shown to provide precise

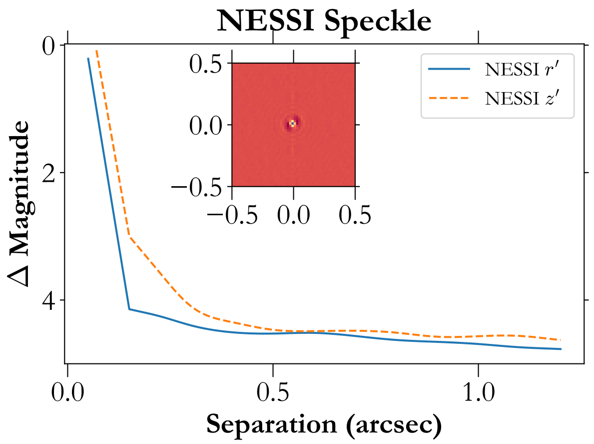

Figure 4. 5σ contrast curve for TOI-7149 observed from NESSI in the Sloan r'filter and z'filter showing no bright companions within 1.″2 from the host star. The z' image is shown as an inset 1 across.

wavelength calibration and drift correction at the 30 cm s^{-1} level (G. Stefansson et al. 2020).

We use the template-matching method (G. Anglada-Escudé & R. P. Butler 2012) implemented under the `SpEctrum Radial Velocity AnaLyser` pipeline (M. Zechmeister et al. 2018; G. Stefánsson et al. 2023) to extract RVs, which has been modified for HPF (G. Stefansson et al. 2020). We used `barycorrpy` (S. Kanodia & J. Wright 2018) to perform the barycentric correction on the individual spectra, which is the Python implementation of the algorithms from J. T. Wright & J. D. Eastman (2014). Each visit consisted of two exposures of 969 s each that were subsequently combined by weighted averaging. The median signal-to-noise ratio at 1070 nm per exposure is 21 per 1D extracted pixel, and the median RV uncertainty per visit (binned) is 40 m s^{-1}. The RVs used in our analysis are listed in Table 1. A generalized Lomb–Scargle (GLS) periodogram (N. R. Lomb 1976; J. D. Scargle 1982; M. Zechmeister & M. Kürster 2009) of the RVs (Figure 6) shows a significant peak at the planetary orbital period (<0.1% false alarm probability).

3. Stellar Parameters

3.1. Spectroscopic Parameters from HPF

We used the `HPF-SpecMatch`[24] package (G. Stefansson et al. 2020) to derive the stellar effective temperature (T_e), surface gravity ($\log g_\star$), metallicity ([Fe/H]), and rotational velocity ($v \sin i_\star$) from the observed high-resolution spectra of TOI-7149. `HPF-SpecMatch` empirically derives spectroscopic parameters (e.g., S. W. Yee et al. 2017) by using a weighted linear combination of the five stellar spectra from a library of well-characterized stars that best-match the target star. The HPF spectral library used in this work consisted of 100 stars with parameters covering $2700\,\mathrm{K} \leqslant T_e \leqslant 4500\,\mathrm{K}$, $4.63 < \log g_\star < 5.26$, and $-0.49 < [\mathrm{Fe/H}] < 0.53$. We analyzed the spectral region between 8534 and 8645 Å because of the minimal telluric contamination. The uncertainties reported were the standard deviation of the residuals from a leave-one-out cross-validation procedure applied to the library (see more details in G. Stefansson et al. 2020). Our analysis determined $T_e = 3363$ 59 K, $\log g_\star = 4.88 \pm 0.04$,

---

[24] https://gummiks.github.io/hpfspecmatch/

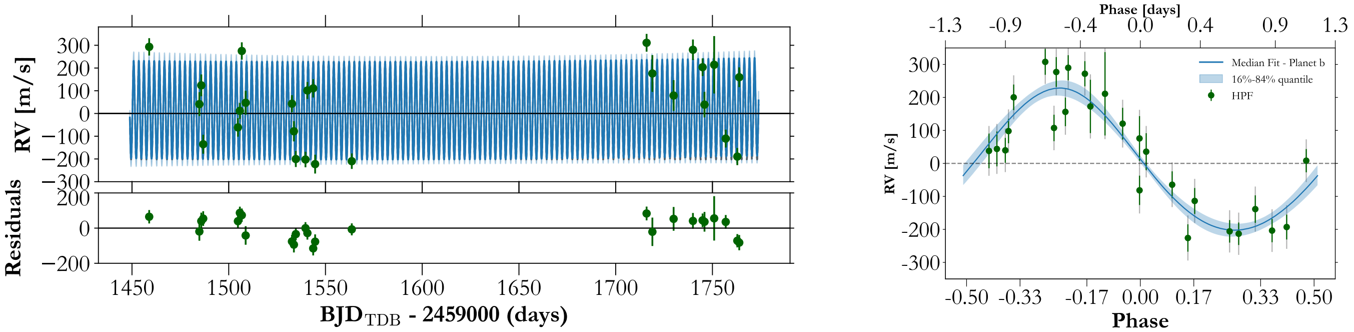

Figure 5. Left: Time series RVs of TOI-7149 with HPF data shown in green, and the best-fitting model derived from the joint fit to the photometry and RVs plotted in blue. The model includes the 16%–84% confidence interval in lighter blue, as well as the RV trend detailed in Table 3. The bottom panel shows the residuals after subtracting the model from the data. Right: HPF RV observations phase-folded to the best-fit orbital period from the joint fit described in Section 4. Instrument error bars are shown in green, while RV jitter added in quadrature is shown in the background on each point in gray.

Table 1
RVs (Binned in   30 Minutes Exposures) of TOI-7149

BJD$_{\mathrm{TDB}}$ (d)	RV (m s^{-1})	σ (m s^{-1})
2460458.89432	244.11	38.14
2460484.82215	−7.78	52.54
2460485.82212	74.79	47.94
2460486.81456	−184.16	41.68
2460504.75701	−110.25	40.53
2460505.76022	−37.42	35.21
2460506.75608	226.04	38.05
2460508.74988	−1.80	52.77
2460532.68146	−6.02	37.62
2460533.68560	−127.25	44.42
2460534.67720	−249.30	35.16
2460539.66378	−251.55	34.12
2460540.66150	52.33	37.00
2460543.65399	61.72	40.08
2460544.65574	−271.69	41.43
2460563.60016	−258.84	34.07
2460715.97255	261.99	39.13
2460718.96233	127.00	80.73
2460729.93788	30.04	67.57
2460739.92359	231.29	45.14
2460744.90921	154.57	38.72
2460745.90062	−10.17	56.00
2460750.89637	165.26	126.27
2460756.87158	−159.44	39.20
2460762.86392	−238.50	37.73
2460763.86039	110.51	43.37

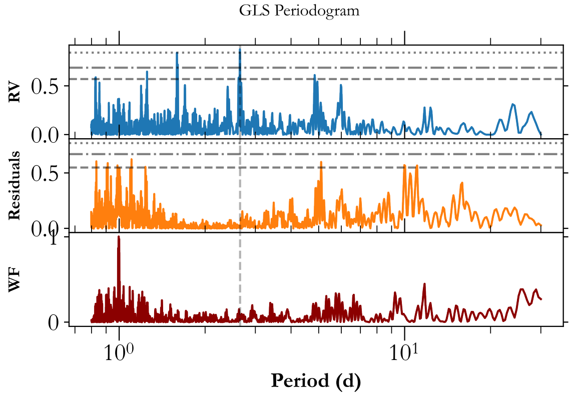

Figure 6. Top: GLS of the HPF RVs in blue, with the dashed vertical line showing the planetary orbital period. The horizontal lines are the 10%, 1%, and 0.1% false alarm probability levels. There is a peak in the RV periodogram, corresponding to the orbital period, that is significant at the <0.1% level. Middle: GLS of the residuals obtained after subtracting the best-fit model do not display any significant peaks. Bottom: Window function of the HPF RVs showing the characteristic 1.0 day peak indicative of observing cadence at HET.

and $[\mathrm{Fe/H}] = -0.08 \quad 0.16$ for TOI-7149. `HPF-SpecMatch` could only place a upper limit of $v \sin i_\star < 2$ km s^{-1}, which is consistent with the lack of rotation signal in TESS or HPF activity indicators, thereby suggesting an old inactive star (>1 Gyr).

3.2. Stellar Parameters from the Spectral Energy Distribution

We followed the procedures in C. I. Cañas et al. (2023) to derive stellar parameters using the `EXOFASTv2` analysis package (J. D. Eastman et al. 2019) to model the spectral energy distribution (SED). `EXOFASTv2` models the observed magnitudes using the MIST model grids (J. Choi et al. 2016; A. Dotter 2016) and uses the $R_v = 3.1$ reddening law from E. L. Fitzpatrick (1999) to calculate a visual magnitude extinction. We applied Gaussian priors on the (i) broadband optical and near-infrared photometry listed in Table 2, (ii) spectroscopic parameters from `HPF-SpecMatch`, and (iii) parallax from Gaia DR3 (Gaia Collaboration et al. 2023). We used a uniform prior on the visual extinction (A_V) with an upper limit derived from the estimates by G. M. Green et al. (2019) at the location of TOI-7149. The stellar parameters are presented in Table 2. TOI-7149 has a mass and radius of $M_\star = 0.344 \quad 0.030\, M_\odot$ and $R_\star = 0.351 \quad 0.015\, R_\odot$, respectively. The T_{eff} estimate from SED photometry is 3237   K, which is about 2σ lower than our spectroscopic estimate. However, for this work we choose the spectroscopic `HPF-SpecMatch` estimates.

We use the color–magnitude relations in Table 4 from R. Kiman et al. (2019) and Table 7 from C. Cifuentes et al. (2020) to estimate the spectral subtype of TOI-7149 using Gaia and 2MASS photometry as a fully convective M4 dwarf.

3.3. Galactic Kinematics

We use the systemic velocity from HPF and astrometry from Gaia DR3 to calculate the *UVW* velocities[25] in the barycentric frame using `GALPY` (J. Bovy 2015), which are listed in Table 2. Using the BANYAN tool

---

[25] With *U* toward the Galactic center, *V* toward the direction of Galactic spin, and *W* toward the North Galactic Pole (D. R. H. Johnson & D. R. Soderblom 1987).

Table 2
Summary of Stellar Parameters for TOI-7149

Parameter	Description	Value	References
Main identifiers:			
TOI	TESS object of interest	7149	TESS mission
TIC	TESS input catalog	459323923	Stassun
2MASS	⋯	J16185724+1910327	2MASS
Gaia DR3	⋯	1200751810900182400	Gaia DR3
Equatorial coordinates and proper motion:			
$_{\rm J2000}$	R.A.	244.738 0.034	Gaia DR3
$_{\rm J2000}$	decl.	19.176 0.028	Gaia DR3
μ	Proper motion (R.A., mas yr^{-1})	−7.698 0.039	Gaia DR3
μ	Proper motion (decl., mas yr^{-1})	12.882 0.041	Gaia DR3
ϖ	Parallax in mas	7.86 0.05	Gaia DR3
G	G mag	16.1324 0.0007	Gaia DR3
$A_{V,\rm max}$	Maximum visual extinction	0.274	Green
Optical and near-infrared magnitudes:			
g'	PS1 g' mag	18.08 0.01	PS1
r'	PS1 r' mag	16.87 0.02	PS1
i'	PS1 i' mag	15.409 0.005	PS1
z'	PS1 z' mag	14.746 0.008	PS1
y'	PS1 y' mag	14.41 0.01	PS1
J	J mag	13.16 0.03	2MASS
H	H mag	12.47 0.03	2MASS
K_s	K_s mag	12.23 0.02	2MASS
$W1$	WISE1 mag	12.027 0.098	WISE
$W2$	WISE2 mag	11.914 0.022	WISE
$W3$	WISE3 mag	12.045 0.284	WISE
Spectroscopic parameters:[a]			
$T_{\rm eff}$	Effective temperature in K	3363 59	This work
[Fe/H]	Metallicity in dex	−0.08 0.16	This work
$\log(g)$	Surface gravity in cgs units	4.88 0.04	This work
$v \sin i_\star$	Rotational broadening (km s^{-1})	<2	This work
Model-dependent stellar SED and isochrone fit parameters:[b]			
M_*	Mass in $M_\odot$	0.344 0.030	This work
R_*	Radius in $R_\odot$	0.351 0.015	This work
L_*	Luminosity in $L_\odot$	0.01215 0.00063	This work
ρ_*	Density in g cm^{-3}	11.2 1.0	This work
Age	Age in Gyr	7.8 5.0	This work
Distance	Distance in pc	127.24 0.74	This work
A_v	Visual extinction in mag	$0.100^{+0.037}_{-0.058}$	This work
Other stellar parameters:			
ΔRV	"Absolute" RV in km s^{-1}	−36.7 0.5	This work
U, V, W	Galactic velocities in km s^{-1}	−26.47 0.31, −7.67 0.22, −25.87 0.33	This work
U, V, W[c]	Galactic velocities (LSR) in km s^{-1}	−15.37 0.90, 4.57 0.72, −18.62 0.69	This work

Notes. References are: Gaia DR3 (Gaia Collaboration et al. 2023), Green (G. M. Green et al. 2019), Stassun (K. G. Stassun et al. 2018), 2MASS (R. M. Cutri et al. 2003), PS1 (DR2; K. C. Chambers et al. 2016).
[a] Derived using the HPF spectral matching algorithm from G. Stefansson et al. (2020).
[b] `EXOFASTv2` derived values using MIST isochrones with the Gaia parallax and spectroscopic parameters in *a*) as priors.
[c] The barycentric UVW velocities are converted into local standard of rest (LSR) velocities using the constants from R. Schönrich et al. (2010).

(J. Gagné et al. 2018), we classify TOI-7149 as a field star in the thin disk (T. Bensby et al. 2014).

3.4. Stellar Companions

Gaia DR3 (Gaia Collaboration et al. 2023) provides an astrometric constraint on the lack of unresolved companions using the renormalized unit weight error (RUWE) metric. For TOI-7149, the reported RUWE is 0.973, which is lower than the commonly accepted threshold in the literature of $\gtrsim$1.4 to ascertain the potential presence of stellar companions in binary studies (V. Belokurov et al. 2020; Z. Penoyre et al. 2020). Similarly, there is no significant astrometric excess noise reported alongside the Gaia astrometry. Finally, the host star is not part of a bound pair as determined from the Gaia catalog of K. El-Badry et al. (2021). This is consistent with the lack of any bright companions from speckle imaging in Section 2.3 and, together, suggests that TOI-7149 is a single-star.

4. Joint Fitting of Photometry and RVs

Similar to previous discoveries from our Searching for GEMS survey, we perform a joint fit of the photometry and RVs using the `Python` package `exoplanet` (D. Foreman-Mackey et al. 2021b) which uses `PyMC3`, the Hamiltonian Monte Carlo package (J. Salvatier et al. 2016).

We use a quadratic limb-darkening law with coefficients derived using the reparametrization suggested by D. M. Kipping (2013). Each instrument (TESS, Palomar, RBO, LCRO, and TMMT) has separate limb-darkening coefficients. Due to TESS's large pixels and the presence of background stars, we included a dilution term for each TESS sector and placed a uniform prior between 0.001 and 1.5 (explained in S. Kanodia et al. 2023c), such that the transit depth was determined using the other photometric data sets where the stars are spatially well-resolved and excluded from the apertures used to derive the photometry. We also included an RV jitter (white noise), RV offset (γ), and quadratic RV trend in the fit. The orbital eccentricity is consistent with circular (<0.12, <0.17, <0.22, at 1, 2, 3σ, respectively), especially when considering the Lucy–Sweeney bias (L. B. Lucy & M. A. Sweeney 1971). The derived parameters for this system are listed in Table 3. The measured RV trend is consistent with 0 (i.e., a flat line, at $<1\sigma$). The phase-folded transit photometry and best-fit models (and uncertainty) are shown in Figure 3. The RV time series and phase-folded fit are shown in Figure 5.

Table 3
Derived Parameters for the TOI-7149 System

Parameter	Units	Value[a]
Orbital parameters:		
Orbital period	P (days)	2.65206166 0.00000080
Eccentricity	e	$0.078^{+0.047}_{-0.048}$
Argument of periastron	ω (radians)	$-0.286^{+0.692}_{-0.587}$
Semi-amplitude velocity	K (m s^{-1})	216 21
Systemic velocity[b]	$\gamma_{\rm HPF}$ (m s^{-1})	-49 17
RV trend	$dv\ /\ dt$ (m s^{-1} yr^{-1})	13^{+44}_{-42}
	d^2v/dt^2 (m s^{-1} yr^{-2})	52^{+96}_{-98}
RV jitter	$\sigma_{\rm HPF}$ (m s^{-1})	55^{+15}_{-13}
Transit parameters:		
Transit midpoint	T_C (BJD$_{\rm TDB}$)	2459703.596050 0.00029
Scaled radius	R_p/R_*	$0.3334^{+0.0048}_{-0.0053}$
Scaled semimajor axis	a/R_*	$15.52^{+0.67}_{-0.54}$
Orbital inclination	i (deg)	$89.25^{+0.39}_{-0.28}$
Transit duration	T_{14} (days)	$0.0719^{+0.0025}_{-0.0030}$
Dilution[c]	$D_{\rm TESSS25}$	1.074 0.035
	$D_{\rm TESSS51}$	1.17 0.04
	$D_{\rm TESSS52}$	1.21 0.04
	$D_{\rm TESSS79}$	1.12 0.034
Limb darkening[d]	$(u_1, u_2)_{\rm TESS}$	$0.36^{+0.27}_{-0.23}$, $0.47^{+0.28}_{-0.38}$
	$(u_1, u_2)_{\rm RBO}$	$0.19^{+0.19}_{-0.13}$, $0.26^{+0.29}_{-0.30}$
	$(u_1, u_2)_{\rm TMMT}$	$0.37^{+0.33}_{-0.26}$, $0.10^{+0.37}_{-0.30}$
	$(u_1, u_2)_{\rm LCRO}$	$0.37^{+0.32}_{-0.25}$, $0.06^{+0.35}_{-0.26}$
	$(u_1, u_2)_{\rm Palomar}$	0.28 0.17, $0.19^{+0.32}_{-0.29}$
Planetary parameters:		
Mass	M_p (M)	224 24
	M_p ($M_{\rm J}$)	0.705 0.075
Radius	R_p (R)	13.2 0.51
	R_p ($R_{\rm J}$)	1.18 0.045
Density	ρ_p (g cm^{-3})	$0.530^{+0.085}_{-0.069}$
Semimajor axis	a (au)	$0.02603^{+0.00071}_{-0.00076}$
Average incident flux[e]	$\langle F$ (10^5 W m^{-2})	0.280 0.040
Planetary insolation	S (S)	20.6 2.9
Equilibrium temperature[f]	$T_{\rm eq}$ (K)	593 21

Notes.
[a] The reported values refer to the 16%–50%–84% percentile of the posteriors.
[b] RV offset in addition to the "Absolute RV" from Table 2.
[c] Dilution over-correction in `tglc` from background stars in TESS, constrained using ground-based apertures.
[d] Where $u_1 + u_2 < 1$, and $u_1 > 0$ according to D. M. Kipping (2013).
[e] We use a Solar flux constant = 1360.8 W m^{-2}, to convert insolation to incident flux.
[f] We assume the planet to be a blackbody with zero albedo and perfect energy redistribution to estimate the equilibrium temperature.

5. Discussion

5.1. TOI-7149 b Compared to Other GEMS

To contextualize TOI-7149 b with respect to other transiting planets, especially transiting GEMS, we queried the NASA Exoplanet Archive Planetary Systems Data Table on 2025 April 11 (R. L. Akeson et al. 2013; NASA Exoplanet Archive 2025). To this, we add TOI-7149 b (this work), TOI-6330 b and TOI-6303 b (A. Hotnisky et al. 2024), TOI-5573 b (R. B. Fernandes et al. 2025), TOI-5349 b (A. Sandoval et al. 2025, in preparation), and TOI-5916 b (S. O'Brien & A. Wong et al. 2025, in preparation).[26] To focus on FGKM host stars, we exclude planets with hosts >7200 K or $>1.5 M_\odot$. Furthermore, we limit the sample to planets with radii $\gtrsim 8\ R$ within 1σ ($\gtrsim 0.7\ R_{\rm J}$), radius precision $>5\sigma$, and mass precision $>3\sigma$. This results in 544 transiting giant planets that are shown in Figure 7, of which 30 are transiting GEMS. We show that TOI-7149 is one of the lowest mass stars to host a transiting giant planet.

TOI-7149 b is a fully convective M-dwarf, as can be seen from its location (Figure 8) below the transition between partially and fully convective M-dwarfs (W.-C. Jao et al. 2018). This gap marks the convective instability brought about by fluctuations in ^{3}He fusion and episodic cycling therein (J. L. van Saders & M. H. Pinsonneault 2012; I. Baraffe & G. Chabrier 2018; J. MacDonald & J. Gizis 2018; G. A. Feiden et al. 2021). Furthermore, this gap is associated with luminosity and temperature variations for stars within the narrow strip, as well as marked differences between the flare rates and activity levels on both sides of it (W.-C. Jao et al. 2023; W.-C. Jao & A. Youngblood 2025). Additionally, Figure 8 shows that a number of transiting GEMS are above the main-sequence and may be metal-rich, as indicated by their location with respect to the PARSEC[27] (A. Bressan et al. 2012; Y. Chen et al. 2014) isochrones. This apparent preference for GEMS to orbit metal-rich stars is consistent with findings from T. Gan et al. (2025) and R. Rodríguez Martínez et al. (2023). We note that TOI-7149 appears to be much more metal-rich in the Gaia color–magnitude diagram (CMD) as compared to our `HPF-SpecMatch` metallicity estimates. However, we add the usual caveats regarding M-dwarf metallicities, both from empirical methods such as `HPF-SpecMatch`, as well as synthetic isochrones. These are due to the faintness of the star, the molecular lines erasing the continuum (V. M. Passegger et al. 2022). Furthermore, errors due to interpolating synthetic atmospheres are particularly egregious for M-dwarfs (A. J. Wheeler et al. 2024). Therefore, robust metallicity

---

[26] This work also includes the discovery of TOI-6158 b; however, it is grazing and does not meet our radius precision cuts.
[27] http://stev.oapd.inaf.it/cmd

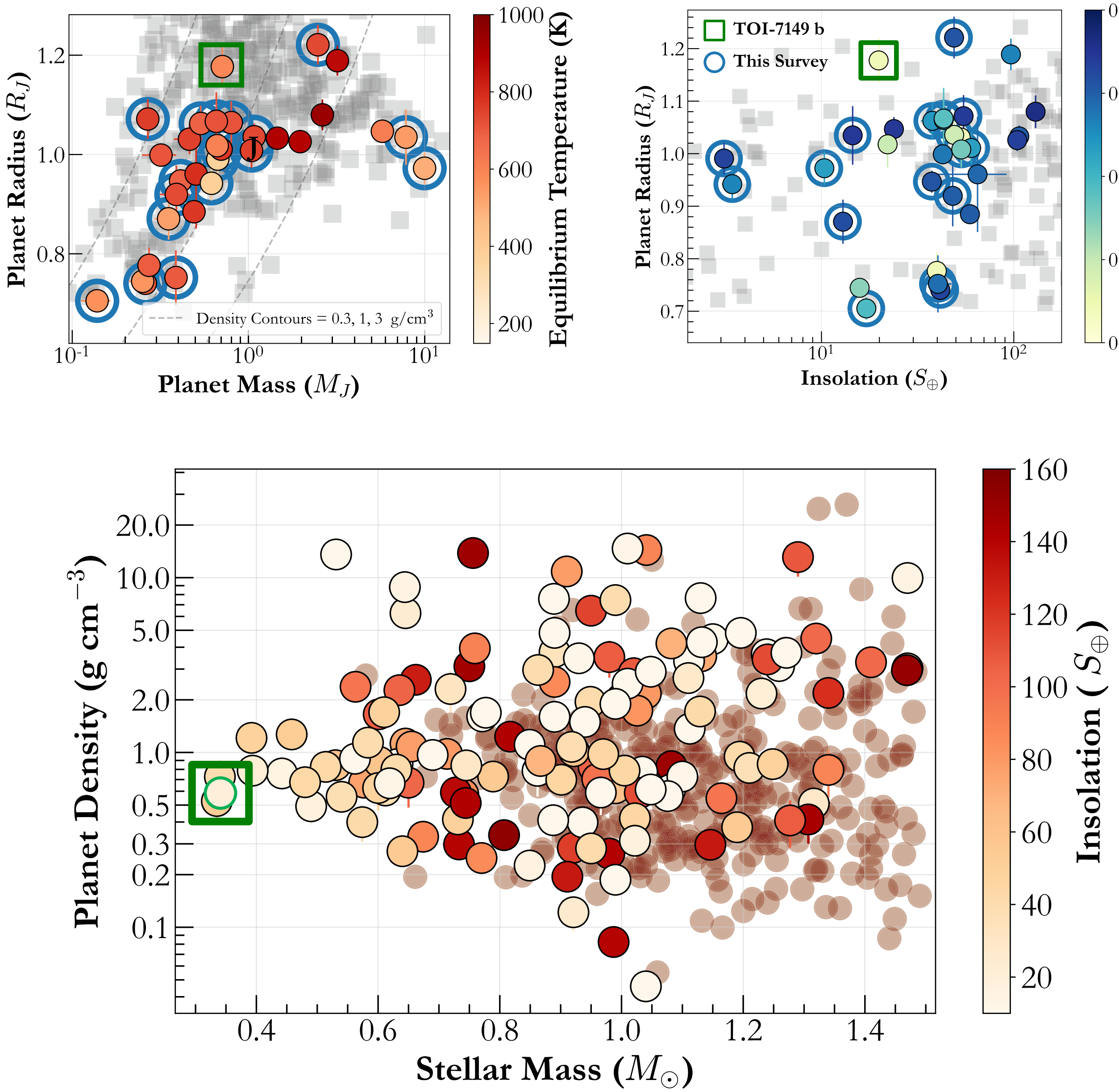

Figure 7. Top Left: TOI-7149 b (green square) in a mass–radius plane alongside other transiting M-dwarf planets (colored by equilibrium temperature). The GEMS discovered by the Searching for GEMS survey are circled in blue. We also include planets around FGK stars in the background, along with density contours for 0.3, 1, 3 g cm^{-3} (NASA Exoplanet Archive 2025). Top Right: The insolation-radius plane is shown for the same sample of planets. Bottom: Bulk planetary density vs. stellar mass, color coded by insolation flux. Warm Jupiters orbiting FGK dwarfs receiving <160 $S_\oplus$ (T_{eq} ≲ 1000 K) flux are shown in solid color, with hot Jupiters in the background (red circles). TOI-7149 is one of the lowest mass stars hosting a transiting giant planet.

dependence studies for these planets necessitate a homogeneous analysis of the host-star metallicities within a consistent framework, which is currently beyond the scope of this work.

5.2. *TOI-7149 b Appears to be Inflated*

TOI-7149 b appears to be quite inflated at ≈1.2 R_J, though the mechanism causing this for either planet is not currently known. We verified this by using `planetsynth` (S. Müller & R. Helled 2021) synthetic planetary evolution tracks and predicting the radius for TOI-7149 b based on its mass, insolation flux, and assuming different bulk metallicities (Figure 9). The predicted planetary radii (≈1R_J) are all inconsistent with the measured radius of 1.18 ± 0.045R_J and the old age (>>1 Gyr) of the host star suggested by its lack of activity. TOI-7149 b is hence likely inflated despite its insolation flux (20 $S_\oplus$) being much lower than the 160 $S_\oplus$ threshold, above which radius inflation seen for hot Jupiters (D. P. Thorngren & J. J. Fortney 2018). Thus, it necessitates some additional source of heating, or delay in cooling, to explain its structure.

5.3. *Future Characterization to Explore the Inflated Nature of TOI-7149 b*

The low density and inflated nature of TOI-7149 b make it a valuable target for future atmospheric characterization (TSM ≈ 132; ESM ≈ 78). Emission spectroscopy can measure the

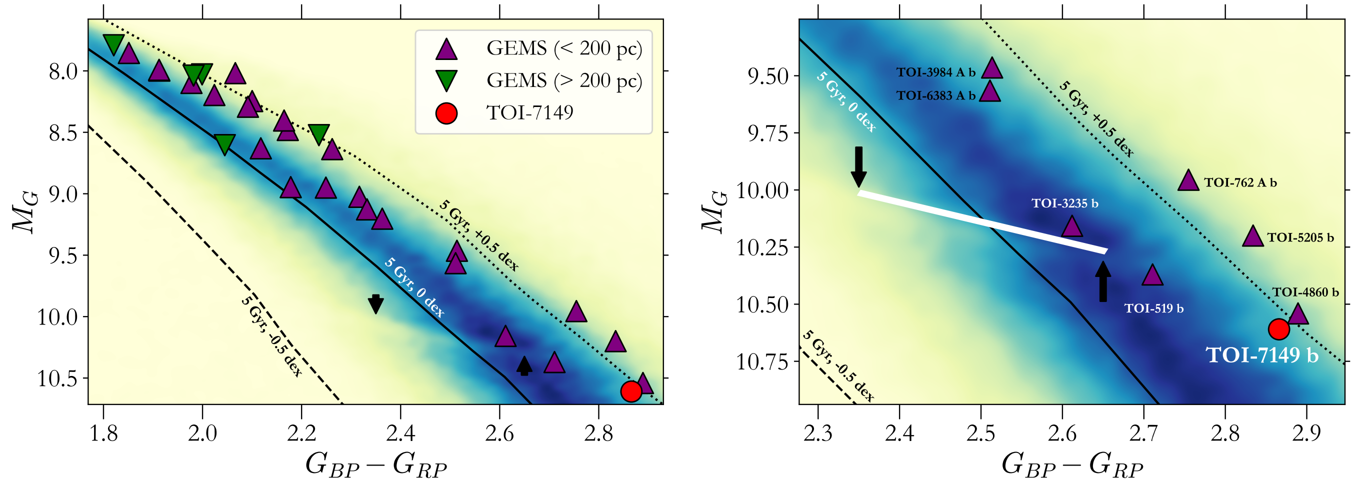

Figure 8. We show a Gaia CMD for the 200 pc sample from the Searching for GEMS survey with a Gaussian kernel density estimation, which is darker in regions with more stars. The upright violet triangles indicate GEMS within 200 pc, whereas the inverted green ones have distances >200 pc. The red dot shows TOI-7149, which is the one of the coldest and reddest M-dwarfs to host one of these GEMS. We also overplot the PARSEC isochrones for a 5 Gyr system at +0.5, 0 and −0.5 dex metallicity (A. Bressan et al. 2012; Y. Chen et al. 2014). The white strip and black arrows indicate the upper edge of the convective transition between partially and fully convective M-dwarfs (W.-C. Jao et al. 2018). The full extent of the CMD is shown on the left, whereas on the right we zoom into the region near the transition zone to show other similar stars to TOI-7149.

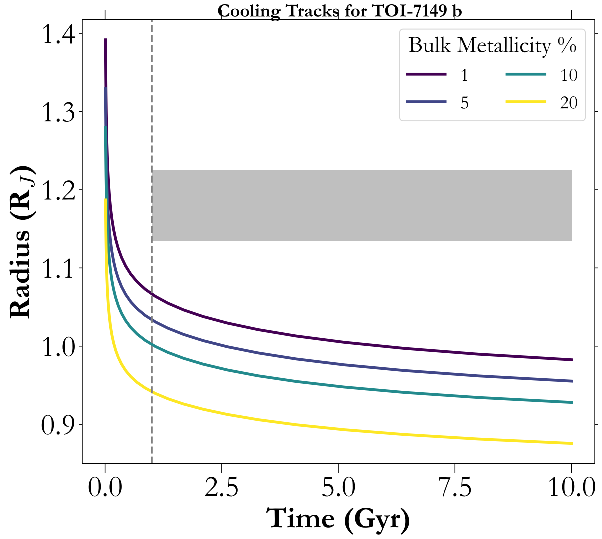

Figure 9. The gray bar shows the 1σ radius measurement along with age estimates >1 Gyr. The different color cooling tracks generated from `planetsynth` assume the minimum atmospheric metallicity of solar (1.2%) and different bulk metallicities. Takeaway: The measured radius for TOI-7149 b is inconsistent with theoretical model predictions, thereby suggesting that it is inflated.

thermal emission from the planet, and hence its effective temperature[28] ($T_{\rm eff}$; e.g., GJ436 b; M. Agúndez et al. 2014), which coupled with its equilibrium temperature provides an estimate of the internal temperature ($T_{\rm int}^4 \simeq {T_{\rm eff}}^4 - T_{\rm eq}^4$). This estimate of the internal temperature and heat flux is expected to be higher than predictions from cooling tracks (similar to Figure 9). Conversely, an internal temperature consistent with cooling tracks would suggest the absence of additional heating, and perhaps necessitate aerosols that provide opacity at high-altitudes, and hence a larger radius. The large planet-to-stellar radius ratio and cool host star result in a large eclipse depth (Figure 10), making it suitable for eclipse observations with ARIEL (G. Tinetti et al. 2016; R. Helled et al. 2022) and JWST MIRI/LRS (G. H. Rieke et al. 2015; G. S. Wright et al. 2023). Given that measurements of the internal temperature (e.g., WASP-107 b; L. Welbanks et al. 2024) of GEMS via transmission spectroscopy are often confounded by the transit light source effect (B. V. Rackham et al. 2018; C. I. Cañas et al. 2025), eclipse measurements may be a more suitable temperature probe.

5.4. Sample Analysis with `MRExo`

Aided by this discovery of TOI-7149 b as well as recent giant exoplanets around mid M-dwarfs—TOI-519 b (H. Parviainen et al. 2021; T. Kagetani et al. 2023), TOI-4860 b (J. M. Almenara et al. 2024; A. H. M. J. Triaud et al. 2023), TOI-5205 b (S. Kanodia et al. 2023c), TOI-3235 b (M. J. Hobson et al. 2023), and TOI-762 A b (J. D. Hartman et al. 2024)—we compare bulk properties of transiting giant planets across stellar masses. This is one of the primary goals of the Searching for GEMS survey, i.e., to quantify differences between giant planets orbiting M-dwarfs and FGK stars as a means of constraining giant planet formation.

S. Kanodia (2024) find that transiting GEMS tend to have lower masses than their FGK dwarf warm Jupiter analogues because there are fewer super-Jupiters ($\gtrsim 2\ M_{\rm J}$) known to orbit M-dwarfs. Once super-Jupiters are excluded from the analysis to focus on giant planets that ostensibly form through core accretion ($<$2–4 $M_{\rm J}$; N. C. Santos et al. 2017; K. C. Schlaufman 2018), the mean mass of transiting warm Jupiters is independent of stellar mass. This lack of dependence of warm Jupiter masses on host-star mass was hypothesized to suggest that there is a minimum disk mass threshold that dominates the outcome of the core-accretion formation paradigm (H. Mizuno 1980; J. B. Pollack et al. 1996; G. Laughlin et al. 2004). S. Kanodia (2024) hypothesized that this threshold, when compared to ALMA measurements of protoplanetary disk masses, would explain the lower

---

[28] Note that this is distinct from the stellar effective temperature, but refers to a similar concept for the planet as determined by its thermal emission. This can be and is usually different from the equilibrium temperature ($T_{\rm eq}$), which in this context is akin to the irradiation temperature (or the expected temperature of the planet based on the flux it receives). If a planet has no internal source of heat ($T_{\rm int}$ 0), then $T_{\rm eff} \simeq T_{\rm eq}$.

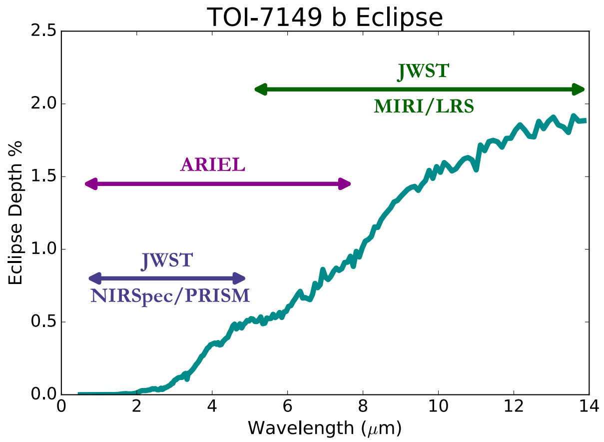

Figure 10. Simulated emission spectrum of TOI-7149 b, also showing the instrument bandpasses for JWST NIRSpec and MIRI, along with ARIEL.

occurrence of transiting GEMS compared to their FGK dwarf counterparts (E. M. Bryant et al. 2023; T. Gan et al. 2023) and these trends observed in their bulk properties. We emphasize that the nature of this work, i.e., comparing conditional probability distributions, is agnostic to the absolute occurrence of transiting giant planets as a function of stellar mass (Section 2.2; S. Kanodia 2024).

Following the methodology described in S. Kanodia et al. (2024a) and S. Kanodia (2024), we used the *n*-dimensional nonparametric sample inference framework `MRExo` (S. Kanodia et al. 2023b), which utilizes a convolution of normal and beta-density functions, to model the joint density of planets (B. Ning et al. 2018; S. Kanodia et al. 2019). Regions of parameter space with more planets have a higher joint probability. This *n*-dimensional joint distribution can then be marginalized to estimate the normalized conditional distribution to study the interdependence of parameters. The degree of the beta-density functions characterizes the complexity of the model required to fit the data.

We extended the analysis to additional dimensions and probed the impact of insolation flux and stellar mass on planetary bulk densities. Given that hot Jupiters with high insolation fluxes tend to be inflated due to Ohmic dissipation (T. Guillot & A. P. Showman 2002; L. M. Weiss et al. 2013; D. P. Thorngren & J. J. Fortney 2018), their bulk densities cannot be trivially connected to their heavy-element (metal) content (D. P. Thorngren et al. 2016; S. Müller & R. Helled 2023). We therefore limited this analysis to the aforementioned sample of warm Jupiters and fit its probability density in three dimensions—M_*, ρ_p, and S_p (stellar mass, bulk density, and insolation). We used *k*-fold cross validation to estimate the optimum number of degrees for the beta polynomials (Appendix C; S. Kanodia et al. 2023b) as 72, 41, and 72, respectively.

We first fit this to all the 544 giant planets in our sample, the results of which are shown in Figure 11. We marginalized the distribution at $50\,S$ (700 K, assuming 0 albedo) since that is the median insolation flux for transiting GEMS discovered so far. Thus, we calculated the 1D probability distribution of planetary densities as a function of stellar mass from mid M-dwarfs to the Kraft break (0.4–1.3 $M_\odot$). This upper limit for stellar masses considered is to avoid the potential observational biases due to the increase in $v \sin i_\star$ of stars above the Kraft break (Section 5.3; S. Kanodia 2024). This conditional probability—$f(\rho|S_p = 50\,S\ \ , M_*)$—gave us the expected planetary density for warm Jupiters receiving $50\,S$ from a range of host-star masses.

Next, we imposed an upper limit on the planetary mass of the input sample to investigate whether the outcomes of planet formation might be sensitive to this threshold. We test limits of $4\,M_{\rm J}$, $3\,M_{\rm J}$, $2.5\,M_{\rm J}$, and $2\,M_{\rm J}$, and we show the results for the $4\,M_{\rm J}$ and $2\,M_{\rm J}$ thresholds in Figure 12. Similar to previous results studying trends in planetary mass, we see that for planets with masses below 2 $M_{\rm J}$, the planetary bulk density appears to be agnostic to the host-star mass. This is consistent with the scatter plot of the input sample seen in Figure 7(c), with transiting giant planets seeming to converge toward ρ_p 0.8 g cm^{-3} in bulk density across the stellar mass axis.

We account for the uncertainty due to the sparsity of the sample by performing 100 bootstraps (with replacement), and show the results for the three cases in Figure 12. We compare the mean of each of these distributions $f(\rho|S_p = 50\,S\ \ , M_*)$ using Welch's t-test (B. L. Welch 1947; G. D. Ruxton 2006) and find consistency across the stellar mass axis.

Instead of marginalizing for a single insolation flux, we also repeat this analysis on warm Jupiters with $S_p < 160\,S$ (shown in solid in Figure 7(c)), and find a similar result, with $f(\rho|M_*)$ being constant for the $<2M_{\rm J}$ sample, but varying with stellar mass for the combined sample due to the varying occurrence super-Jupiters and Jupiters as a function of stellar mass (Figure 13). We add the caveat that while planet density is a reasonable proxy for bulk metallicity, it might not necessarily be so if there are systematic differences in the ages, formation and cooling history, or atmospheric composition across the stellar mass axis for giant planets, as suggested by S. Müller & R. Helled (2025) and being investigated with a JWST survey of GEMS (S. Kanodia et al. 2023a).

5.5. *Implications of Lack of Dependence of Bulk Density on Stellar Mass*

We note that under the core-accretion paradigm, upon initiation of the runaway processes—typically assumed to be between 20 and 100 M (R. Helled 2023), depending on the grain size, surface density, gas opacity, and protoplanet gas-to-metal ratio—the protoplanets are expected to exponentially accrete gas from their host disk. This process is only possible until the gas flow to the planet is quenched due to a gap opening up in the disk (D. N. C. Lin & J. C. B. Papaloizou 1993; G. Bryden et al. 1999). Furthermore, given the effect of electron degeneracy pressure beyond Saturn mass ($0.3M_{\rm J}$; D. Saumon et al. 1996), objects in our sample can have masses ranging from Saturn to the Hydrogen-burning mass upper limit while exhibiting a radius comparable to Jupiter. Thus, for the subsample under consideration ($<2M_{\rm J}$), densities ranging from $\rho_{\rm S}$ to $2\rho_{\rm J}$ (0.7–2.6 g cm^{-3}), i.e., a factor of 4, are possible. Yet, we see that the densities of warm Jupiters seem to converge around 0.8 g cm^{-3}.

While this can be interpreted as being consistent with the hypothesis proposed in our previous work (see Figure 8, S. Kanodia 2024), in which a minimum disk mass threshold dictates the final outcome of giant planet bulk densities (as well as their inverse dependent occurrence with stellar mass), we do not account for the impact of migration and evolution during and following formation. Such processes may play a significant role but investigating these effects is beyond the scope of this work.

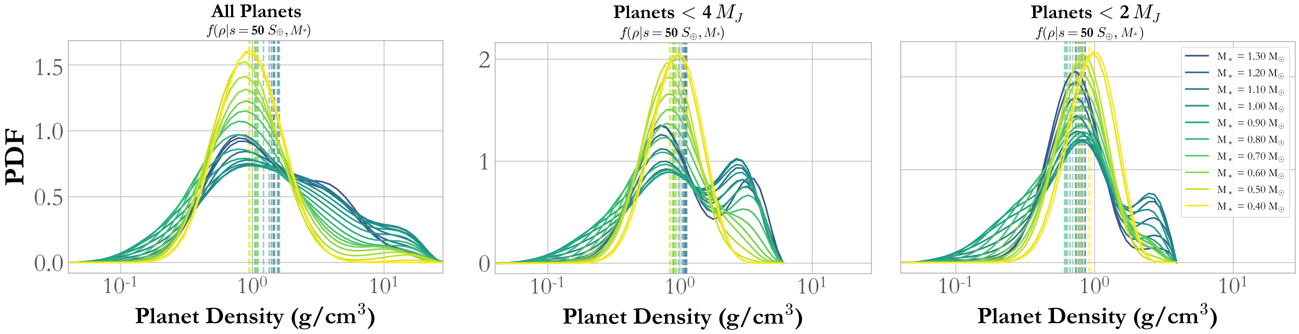

Figure 11. The 3D $f(\rho, S_p, M_*)$ distribution conditioned on different stellar masses and $S_p = 50\,S$ (the median insolation flux for transiting GEMS), to estimate the 1D distribution for $f(\rho|S_p = 50\,S\;\;, M_*)$. In other words, these plots show the probability distribution of bulk densities of transiting giant planets at 50 S across different stellar masses (shown in different colors). The left plot shows the distribution for all the giant planets in our sample. The middle and right plots show similar distributions after excluding planets >4 M_J and >2 M_J from the sample. Takeway: We find that when excluding super-Jupiters (>2 M_J), the bulk density of transiting warm Jupiters (50 S) does not show a strong dependence on host-star mass.

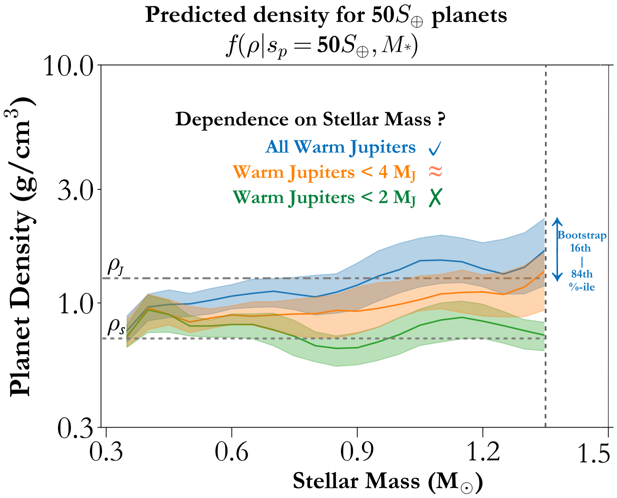

Figure 12. The expectation values for the planetary bulk density as a function of stellar mass for warm Jupiters (50 S), with the shaded regions representing the 16th–84th percentile uncertainty from bootstrapping the samples. The dashed horizontals line show the density of Jupiter and Saturn for reference. We do not display the stellar masses above the Kraft break due to a potential observational bias related to $v \sin i$ and measuring planet masses with RVs. Takeway: For warm Jupiters unaffected by anomalous inflation (D. P. Thorngren & J. J. Fortney 2018), the giant planet bulk densities offer a probe into their heavy-element content, and appear to be independent of host-star mass when super-Jupiters are excluded.

We also note that the absence of a stellar mass dependence for the warm Jupiters with masses $<2M_J$ could potentially indicate a different formation mechanism for planets below this threshold. This has been previously suggested by N. C. Santos et al. (2017), K. C. Schlaufman (2018), and M. Narang et al. (2018) who found a mass upper limit for giant planets around 4–10 M_J and interpreted this boundary as the threshold where the dominant formation mechanism transitions from core accretion to gravitational instability (A. P. Boss 1997).

Overall, this suggests that these GEMS ($<2\,M_J$)—including the ones around mid-to-late M-dwarfs such as TOI-7149 b (this work), TOI-5205 b (S. Kanodia et al. 2023c), and TOI-3235 b (M. J. Hobson et al. 2023), which are a challenge to explain with core accretion due to insufficient disk masses—still likely form in this conventional manner in protoplanetary disks. However, this likely takes place in disks that are very massive for the stars they orbit in order to satisfy the minimum disk mass threshold mentioned above.

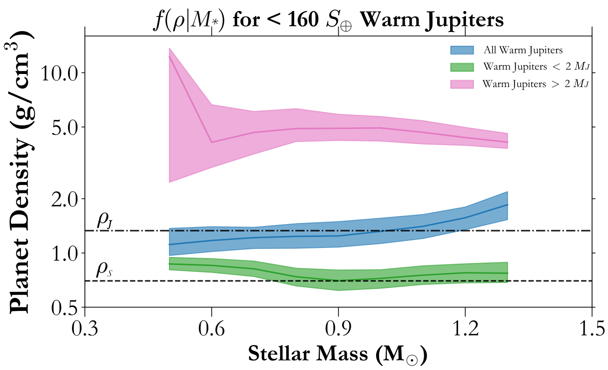

Figure 13. A 2D analysis showing the expectation value for $f(\rho|M_*)$ as well as bootstrapped uncertainties. Similar to Figure 12, we see that the sample of warm Jupiters <160 S (blue; $T_{\rm eq}$ 1000 K) have bulk densities that appear to show a stellar mass dependency. This disappears when considering a sample of planets below <2 M_J (green), suggesting different formation or evolution mechanisms across these two subsamples with contrasting stellar mass dependence. In pink, we also show the super-Jupiters >2 M_J. The large bootstrap uncertainty in this for the M-dwarfs (<0.6$M_\odot$) is driven by the number of super-Jupiters around M-dwarfs (<5). Since the relative number of super-Jupiters to Jupiters increases with increasing stellar mass (Figure 7), the bulk density of the combined sample (blue curve) shows a stellar mass dependence, whereas intrinsically the <2 M_J do not.

6. Summary

As part of the Searching for GEMS survey, we describe the discovery of TOI-7149 b, a low-density planet extending the transiting GEMS sample to lower-mass host stars with a large 12% transit depth. The host star is a fully convective M-dwarf, and one of the coldest to host a gas giant planet. With ground-based RVs from HPF and transits from Palomar, RBO, TMMT, and LCRO, we obtain a precise planetary mass, radius, and planetary density measurement. TOI-7149 b has an inflated radius that cannot be explained by its mass and insolation flux, and can be probed by constraining its internal temperature using emission spectroscopy. We use the statistical framework `MRExo` and extend our analysis from previous work to analyze the sample of transiting warm Jupiters and find a stellar mass dependency for their bulk densities when considering the entire sample of transiting warm Jupiters. This dependency vanishes when focusing on a subset of warm Jupiters with planetary masses $<2M_J$, suggesting (i) different formation pathways for Jupiters below 2 M_J, and (ii) for the $<2M_J$, the formation mechanism seems to be agnostic to the host-star mass. This independence on stellar mass could hint at a minimum threshold disk mass required for giant planet formation, which when contextualized with ALMA disk dust mass measurements in future work could explain the varying occurrence of these objects with stellar mass, as well as the above-mentioned trend.

Acknowledgments

We thank the anonymous referee for the valuable feedback which has improved the quality of this manuscript.

S.K. acknowledges research support from Carnegie Institution of Science through the Carnegie Fellowship. S.K. would like to thank Peter Gao for help with the computing resources that enabled some of these memory intensive `MRExo` analyses to run. S.K. acknowledges feedback from Simon Müller regarding the discussion in this paper.

These results are based on observations obtained with the Habitable-zone Planet Finder Spectrograph on the HET. We acknowledge support from NSF grants AST-1006676, AST-1126413, AST-1310885, AST-1310875, ATI-2009889, ATI-2009554, ATI-2009982, AST-2108512, AST-2108801, and the NASA Astrobiology Institute (NNA09DA76A) in the pursuit of precision RVs in the NIR. The HPF team also acknowledges support from the Heising-Simons Foundation via grant 2017-0494.

The Hobby–Eberly Telescope is a joint project of the University of Texas at Austin, the Pennsylvania State University, Ludwig-Maximilians-Universität München, and Georg-August Universität Gottingen. The HET is named in honor of its principal benefactors, William P. Hobby and Robert E. Eberly. The HET collaboration acknowledges the support and resources from the Texas Advanced Computing Center. We thank the resident astronomers and telescope operators at the HET for the skillful execution of our observations with HPF. We would like to acknowledge that the HET is built on Indigenous land. Moreover, we would like to acknowledge and pay our respects to the Carrizo & Comecrudo, Coahuiltecan, Caddo, Tonkawa, Comanche, Lipan Apache, Alabama-Coushatta, Kickapoo, Tigua Pueblo, and all the American Indian and Indigenous Peoples and communities who have been or have become a part of these lands and territories in Texas, here on Turtle Island.

WIYN is a joint facility of the University of Wisconsin-Madison, Indiana University, NSF's NOIRLab, the Pennsylvania State University, Purdue University, University of California-Irvine, and the University of Missouri.

The authors are honored to be permitted to conduct astronomical research on Iolkam Du'ag (Kitt Peak), a mountain with particular significance to the Tohono O'odham. Data presented herein were obtained at the WIYN Observatory from telescope time allocated to NN-EXPLORE through the scientific partnership of NASA, the NSF, and NOIRLab.

Some of the observations in this paper made use of the NN-EXPLORE Exoplanet and Stellar Speckle Imager (NESSI). NESSI was funded by the NASA Exoplanet Exploration Program and the NASA Ames Research Center. NESSI was built at the Ames Research Center by Steve B. Howell, Nic Scott, Elliott P. Horch, and Emmett Quigley.

This work has made use of data from the European Space Agency (ESA) mission Gaia (https://www.cosmos.esa.int/gaia), processed by the Gaia Data Processing and Analysis Consortium (DPAC, https://www.cosmos.esa.int/web/gaia/dpac/consortium). Funding for the DPAC has been provided by national institutions, in particular the institutions participating in the Gaia Multilateral Agreement.

Computations for this research were performed on the Pennsylvania State University's Institute for Computational and Data Sciences Advanced CyberInfrastructure (ICDS-ACI). This content is solely the responsibility of the authors and does not necessarily represent the views of the Institute for Computational and Data Sciences.

The Center for Exoplanets and Habitable Worlds is supported by the Pennsylvania State University, the Eberly College of Science, and the Pennsylvania Space Grant Consortium.

Some of the data presented in this paper were obtained from MAST at STScI. Specifically, the tglc data products are available as a High Level Science Product (T. Han & T. Brandt 2023). Support for MAST for non-HST data is provided by the NASA Office of Space Science via grant NNX09AF08G and by other grants and contracts.

This work includes data collected by the TESS mission, which are publicly available from MAST. Funding for the TESS mission is provided by the NASA Science Mission directorate.

This research made use of the (i) NASA Exoplanet Archive, which is operated by Caltech, under contract with NASA under the Exoplanet Exploration Program, (ii) SIMBAD database, operated at CDS, Strasbourg, France, (iii) NASA's Astrophysics Data System Bibliographic Services, and (iv) data from 2MASS, a joint project of the University of Massachusetts and IPAC at Caltech, funded by NASA and the NSF.

This research has made use of the SIMBAD database, operated at CDS, Strasbourg, France, and NASA's Astrophysics Data System Bibliographic Services.

This research has made use of the Exoplanet Follow-up Observation Program website, which is operated by the California Institute of Technology, under contract with the National Aeronautics and Space Administration under the Exoplanet Exploration Program

C.I.C. acknowledges support by an appointment to the NASA Postdoctoral Program at the Goddard Space Flight Center, administered by ORAU through a contract with NASA.

The research was carried out, in part, at the Jet Propulsion Laboratory, California Institute of Technology, under a contract with the National Aeronautics and Space Administration (80NM0018D0004).

This research made use of exoplanet (D. Foreman-Mackey et al. 2021b, 2021a) and its dependencies (D. M. Kipping 2013; T. P. Robitaille et al. 2013; J. Salvatier et al. 2016; The Theano Development Team et al. 2016; D. Foreman-Mackey et al. 2017; D. Foreman-Mackey 2018; Astropy Collaboration et al. 2018; R. Kumar et al. 2019; R. Luger et al. 2019; E. Agol et al. 2020).

Facilities: Gaia, HET (HPF), WIYN, RBO, Palomar, TESS, Exoplanet Archive

Software: `ArviZ` (R. Kumar et al. 2019), AstroImageJ (K. A. Collins et al. 2017), `astroquery` (A. Ginsburg et al. 2019), `astropy` (T. P. Robitaille et al. 2013; Astropy Collaboration et al. 2018), `barycorrpy` (S. Kanodia &

J. Wright 2018), `celerite2` (D. Foreman-Mackey et al. 2017; D. Foreman-Mackey 2018), `exoplanet` (D. Foreman-Mackey et al. 2021b, 2021a), `EXOFASTv2` (J. D. Eastman et al. 2019), `HPF-SERVAL` (G. Stefansson et al. 2020), `HPF-SpecMatch` (G. Stefansson et al. 2020), `HxRGproc` (J. P. Ninan et al. 2018), `GALPY` (J. Bovy 2015), `ipython` (F. Pérez & B. E. Granger 2007), `lightkurve` (Lightkurve Collaboration et al. 2018), `matplotlib` (J. D. Hunter 2007), `MRExo` (S. Kanodia et al. 2019, 2023b), `numpy` (T. Oliphant 2006), `pandas` (W. McKinney 2010), `planetsynth` (S. Müller & R. Helled 2021), `PyMC3` (J. Salvatier et al. 2016), `scipy` (T. E. Oliphant 2007; P. Virtanen et al. 2020), `starry` (R. Luger et al. 2019; E. Agol et al. 2020), `tglc` (T. Han & T. D. Brandt 2023), `tessminer` (R. I. Glusman et al. 2025, in preparation), `Theano` (The Theano Development Team et al. 2016), `wotan` (M. Hippke et al. 2019).

ORCID iDs

Shubham Kanodia https://orcid.org/0000-0001-8401-4300
Caleb I. Cañas https://orcid.org/0000-0003-4835-0619
Suvrath Mahadevan https://orcid.org/0000-0001-9596-7983
Andrea S.J. Lin https://orcid.org/0000-0002-9082-6337
Henry A. Kobulnicky https://orcid.org/0000-0002-4475-4176
Ian Karfs https://orcid.org/0009-0009-6263-0490
Andrew Monson https://orcid.org/0000-0002-0048-2586
Arvind F. Gupta https://orcid.org/0000-0002-5463-9980
Michael Rodruck https://orcid.org/0009-0009-4977-1010
Rowen I. Glusman https://orcid.org/0000-0001-9816-0878
Te Han https://orcid.org/0000-0002-7127-7643
William D. Cochran https://orcid.org/0000-0001-9662-3496
Chad F. Bender https://orcid.org/0000-0003-4384-7220
Scott A. Diddams https://orcid.org/0000-0002-2144-0764
Daniel Krolikowski https://orcid.org/0000-0001-9626-0613
Samuel Halverson https://orcid.org/0000-0003-1312-9391
Jessica Libby-Roberts https://orcid.org/0000-0002-2990-7613
Joe P. Ninan https://orcid.org/0000-0001-8720-5612
Paul Robertson https://orcid.org/0000-0003-0149-9678
Arpita Roy https://orcid.org/0000-0001-8127-5775
Christian Schwab https://orcid.org/0000-0002-4046-987X
Guđmundur Stefánsson https://orcid.org/0000-0001-7409-5688

References

Agol, E., Luger, R., & Foreman-Mackey, D. 2020, AJ, 159, 123
Agúndez, M., Venot, O., Selsis, F., & Iro, N. 2014, ApJ, 781, 68
Akeson, R. L., Chen, X., Ciardi, D., et al. 2013, PASP, 125, 989
Almenara, J. M., Bonfils, X., Bryant, E. M., et al. 2024, A&A, 683, A166
Anglada-Escudé, G., & Butler, R. P. 2012, ApJS, 200, 15
Astropy Collaboration, Price-Whelan, A. M., Sipőcz, B. M., et al. 2018, AJ, 156, 123
Baraffe, I., & Chabrier, G. 2018, A&A, 619, A177
Belokurov, V., Penoyre, Z., Oh, S., et al. 2020, MNRAS, 496, 1922
Bensby, T., Feltzing, S., & Oey, M. S. 2014, A&A, 562, A71
Bernabò, L. M., Kanodia, S., Cañas, C. I., et al. 2024, AJ, 168, 273
Bonfils, X., Delfosse, X., Udry, S., et al. 2013, A&A, 549, A109
Boss, A. P. 1997, Sci, 276, 1836
Bovy, J. 2015, ApJS, 216, 29
Bressan, A., Marigo, P., Girardi, Léo, et al. 2012, MNRAS, 427, 127
Bryant, E. M., Bayliss, D., & Van Eylen, V. 2023, MNRAS, 521, 3663
Bryden, G., Chen, X., Lin, D. N. C., Nelson, R. P., & Papaloizou, J. C. B. 1999, ApJ, 514, 344
Cañas, C. I., Kanodia, S., Libby-Roberts, J., et al. 2023, AJ, 166, 30
Cañas, C. I., Lustig-Yaeger, J., Tsai, S.-M., et al. 2025, arXiv:2502.06966
Cañas, C. I., Stefansson, G., Kanodia, S., et al. 2020, AJ, 160, 147
Chambers, K. C., Magnier, E. A., Metcalfe, N., et al. 2016, arXiv:1612.05560
Chen, Y., Girardi, L., Bressan, A., et al. 2014, MNRAS, 444, 2525
Choi, J., Dotter, A., Conroy, C., et al. 2016, ApJ, 823, 102
Cifuentes, C., Caballero, J. A., Cortés-Contreras, M., et al. 2020, A&A, 642, A115
Collins, K. A., Kielkopf, J. F., Stassun, K. G., & Hessman, F. V. 2017, AJ, 153, 77
Cutri, R. M., Skrutskie, M. F., van Dyk, S., et al. 2003, The IRSA 2MASS All-Sky Point Source Catalog (Washington, DC: NASA/IPAC)
Dotter, A. 2016, ApJS, 222, 8
Dressing, C. D., & Charbonneau, D. 2013, ApJ, 767, 95
Eastman, J. D., Rodriguez, J. E., Agol, E., et al. 2019, arXiv:1907.09480
El-Badry, K., Rix, H.-W., & Heintz, T. M. 2021, MNRAS, 506, 2269
Endl, M., Cochran, W. D., Kürster, M., et al. 2006, ApJ, 649, 436
Feiden, G. A., Skidmore, K., & Jao, W.-C. 2021, ApJ, 907, 53
Fernandes, R. B., Kanodia, S., Delamer, M., et al. 2025, AJ, 170, 55
Fitzpatrick, E. L. 1999, PASP, 111, 63
Foreman-Mackey, D. 2018, RNAAS, 2, 31
Foreman-Mackey, D., Agol, E., Ambikasaran, S., & Angus, R. 2017, AJ, 154, 220
Foreman-Mackey, D., Luger, R., Agol, E., et al. 2021a, JOSS, 6, 3285
Foreman-Mackey, D., Savel, A., Luger, R., et al. 2021b, Exoplanet-Dev/Exoplanet v0.4.4, Zenodo, doi:10.5281/zenodo.1998447
Gagné, J., Mamajek, E. E., Malo, L., et al. 2018, ApJ, 856, 23
Gaia Collaboration, Vallenari, A., Brown, A. G. A., et al. 2023, A&A, 674, A1
Gan, T., Theissen, C. A., Wang, S. X., Burgasser, A. J., & Mao, S. 2025, ApJS, 276, 47
Gan, T., Wang, S. X., Wang, S., et al. 2023, AJ, 17, 17
Ginsburg, A., Sipőcz, B. M., Brasseur, C. E., et al. 2019, AJ, 157, 98
Green, G. M., Schlafly, E., Zucker, C., Speagle, J. S., & Finkbeiner, D. 2019, ApJ, 887, 93
Guillot, T., & Showman, A. P. 2002, A&A, 385, 156
Han, T., & Brandt, T. 2023, TESS-Gaia Light Curve ("TGLC"), STScI/MAST, doi:10.17909/610M-9474
Han, T., & Brandt, T. D. 2023, AJ, 165, 71
Hardegree-Ullman, K. K., Cushing, M. C., Muirhead, P. S., & Christiansen, J. L. 2019, AJ, 158, 75
Hartman, J. D., Bayliss, D., Brahm, R., et al. 2024, AJ, 168, 202
Helled, R. 2023, A&A, 675, L8
Helled, R., Werner, S., Dorn, C., et al. 2022, ExA, 53, 323
Henry, T. J., Jao, W.-C., Subasavage, J. P., et al. 2006, AJ, 132, 2360
Hill, G. J., Lee, H., MacQueen, P. J., et al. 2021, AJ, 162, 298
Hippke, M., David, T. J., Mulders, G. D., & Heller, R. 2019, AJ, 158, 143
Hobson, M. J., Jordán, A., Bryant, E. M., et al. 2023, ApJL, 946, L4
Hotnisky, A., Kanodia, S., Libby-Roberts, J., et al. 2024, AJ, 170, 15
Howell, S. B., Everett, M. E., Sherry, W., Horch, E., & Ciardi, D. R. 2011, AJ, 142, 19
Hsu, D. C., Ford, E. B., & Terrien, R. 2020, MNRAS, 498, 2249
Huang, C. X., Vanderburg, A., Pál, A., et al. 2020, RNAAS, 4, 204
Hunter, J. D. 2007, CSE, 9, 90
Jao, W.-C., Henry, T. J., Gies, D. R., & Hambly, N. C. 2018, ApJL, 861, L11
Jao, W.-C., Henry, T. J., White, R. J., et al. 2023, AJ, 166, 63
Jao, W.-C., & Youngblood, A. 2025, AJ, 169, 144
Johnson, D. R. H., & Soderblom, D. R. 1987, AJ, 93, 864
Johnson, J. A., Aller, K. M., Howard, A. W., & Crepp, J. R. 2010, PASP, 122, 905
Kagetani, T., Narita, N., Kimura, T., et al. 2023, PASJ, 75, 713
Kanodia, S. 2024, ApJ, 978, 97
Kanodia, S., Canas, C., Libby-Roberts, J., et al. 2023a, JWST Proposal 3171
Kanodia, S., He, M. Y., Ford, E. B., Ghosh, S. K., & Wolfgang, A. 2023b, ApJ, 956, 76
Kanodia, S., Cañas, C. I., Mahadevan, S., et al. 2024a, AJ, 167, 161
Kanodia, S., Gupta, A. F., Cañas, C. I., et al. 2024b, AJ, 168, 235
Kanodia, S., Halverson, S., Ninan, J. P., et al. 2021, ApJ, 912, 15
Kanodia, S., Mahadevan, S., Libby-Roberts, J., et al. 2023c, AJ, 165, 120
Kanodia, S., Mahadevan, S., Ramsey, L. W., et al. 2018, Proc. SPIE, 10702, 107026Q
Kanodia, S., Wolfgang, A., Stefansson, G. K., Ning, B., & Mahadevan, S. 2019, ApJ, 882, 38
Kanodia, S., & Wright, J. 2018, RNAAS, 2, 4
Kasper, D. H., Ellis, T. G., Yeigh, R. R., et al. 2016, PASP, 128, 105005

Kiman, R., Schmidt, S. J., Angus, R., et al. 2019, AJ, 157, 231
Kipping, D. M. 2013, MNRAS, 435, 2152
Kovács, G., Zucker, S., & Mazeh, T. 2002, A&A, 391, 369
Kumar, R., Carroll, C., Hartikainen, A., & Martin, O. A. 2019, JOSS, 4, 1143
Kunimoto, M., Daylan, T., Guerrero, N., et al. 2022, ApJS, 259, 33
Laughlin, G., Bodenheimer, P., & Adams, F. C. 2004, ApJL, 612, L73
Lightkurve Collaboration, Cardoso, J. V. d. M., Hedges, C., et al., 2018 Lightkurve: Kepler and TESS time series analysis in Python, Astrophysics Source Code Library, ascl:1812.013
Lin, D. N. C., & Papaloizou, J. C. B. 1993, in Protostars and Planets III, ed. E. H. Levy & J. I. Lunine (Tucson, AZ: Univ. Arizona Press), 749
Lomb, N. R. 1976, Ap&SS, 39, 447
Lucy, L. B., & Sweeney, M. A. 1971, AJ, 76, 544
Luger, R., Agol, E., Foreman-Mackey, D., et al. 2019, AJ, 157, 64
MacDonald, J., & Gizis, J. 2018, MNRAS, 480, 1711
Mahadevan, S., Ramsey, L., Bender, C., et al. 2012, Proc. SPIE, 8446, 84461S
Mahadevan, S., Ramsey, L. W., Terrien, R., et al. 2014, Proc. SPIE, 9147, 91471G
Maldonado, J., Villaver, E., Eiroa, C., & Micela, G. 2019, A&A, 624, A94
Masci, F. J., Laher, R. R., Rusholme, B., et al. 2019, PASP, 131, 018003
McKinney, W. 2010, in Proc. 9th Python in Science Conf., ed. S. van der Walt & J. Millman (Austin, TX: SciPy), 56
Metcalf, A. J., Anderson, T., Bender, C. F., et al. 2019, Optic, 6, 233
Mizuno, H. 1980, PThPh, 64, 544
Monson, A. J., Beaton, R. L., Scowcroft, V., et al. 2017, AJ, 153, 96
Müller, S., & Helled, R. 2021, MNRAS, 507, 2094
Müller, S., & Helled, R. 2023, A&A, 669, A24
Müller, S., & Helled, R. 2025, A&A, 693, L4
Narang, M., Manoj, P., Furlan, E., et al. 2018, AJ, 156, 221
NASA Exoplanet Archive 2025, Planetary Systems Composite Parameters, v2025-04-11 00:00, NExScI-Caltech/IPAC, doi:10.26133/NEA13
Ninan, J. P., Bender, C. F., Mahadevan, S., et al. 2018, Proc. SPIE, 0709, 107092U
Ning, B., Wolfgang, A., & Ghosh, S. 2018, ApJ, 869, 5
Oliphant, T. 2006, NumPy: A Guide to NumPy (USA: Trelgol Publishing)
Oliphant, T. E. 2007, CSE, 9, 10
Parviainen, H., Palle, E., Zapatero-Osorio, M. R., et al. 2021, A&A, 645, A16
Pass, E. K., Winters, J. G., Charbonneau, D., et al. 2023, AJ, 166, 11
Passegger, V. M., Bello-García, A., Ordieres-Meré, J., et al. 2022, A&A, 658, A194
Penoyre, Z., Belokurov, V., Wyn Evans, N., Everall, A., & Koposov, S. E. 2020, MNRAS, 495, 321
Pérez, F., & Granger, B. E. 2007, CSE, 9, 21
Pollack, J. B., Hubickyj, O., Bodenheimer, P., et al. 1996, Icar, 124, 62
Rackham, B. V., Apai, D., & Giampapa, M. S. 2018, ApJ, 853, 122
Ramsey, L. W., Adams, M. T., Barnes, T. G., et al. 1998, Proc. SPIE, 3352, 34
Reylé, C., Jardine, K., Fouqué, P., et al. 2021, A&A, 650, A201
Ricker, G. R., Winn, J. N., Vanderspek, R., et al. 2014, JATIS, 1, 014003
Rieke, G. H., Wright, G. S., Böker, T., et al. 2015, PASP, 127, 584
Robitaille, T. P., Tollerud, E. J., Greenfield, P., et al. 2013, A&A, 558, A33
Rodríguez Martínez, R., Martin, D. V., Gaudi, B. S., et al. 2023, AJ, 166, 137
Ruxton, G. D. 2006, BeEco, 17, 688
Sabotta, S., Schlecker, M., Chaturvedi, P., et al. 2021, A&A, 653, A114
Salvatier, J., Wiecki, T. V., & Fonnesbeck, C. 2016, PeerJ Computer Science, 2, e55
Santos, N. C., Adibekyan, V., Figueira, P., et al. 2017, A&A, 603, A30
Saumon, D., Hubbard, W. B., Burrows, A., et al. 1996, ApJ, 460, 993
Scargle, J. D. 1982, ApJ, 263, 835
Schlaufman, K. C. 2018, ApJ, 853, 37
Schlecker, M., Burn, R., Sabotta, S., et al. 2022, A&A, 664, A180
Schönrich, R., Binney, J., & Dehnen, W. 2010, MNRAS, 403, 1829
Scott, N. J., Howell, S. B., Horch, E. P., & Everett, M. E. 2018, PASP, 130, 054502
Stassun, K. G., Oelkers, R. J., Paegert, M., et al. 2019, AJ, 158, 138
Stassun, K. G., Oelkers, R. J., Pepper, J., et al. 2018, AJ, 156, 102
Stefansson, G., Cañas, C., Wisniewski, J., et al. 2020, AJ, 159, 100
Stefansson, G., Hearty, F., Robertson, P., et al. 2016, ApJ, 833, 175
Stefansson, G., Mahadevan, S., Hebb, L., et al. 2017, ApJ, 848, 9
Stefánsson, G., Mahadevan, S., Miguel, Y., et al. 2023, Sci, 382, 1031
The Theano Development Team, Al-Rfou, R., Alain, G., et al. 2016, arXiv:1605.02688
Thorngren, D. P., & Fortney, J. J. 2018, AJ, 155, 214
Thorngren, D. P., Fortney, J. J., Murray-Clay, R. A., & Lopez, E. D. 2016, ApJ, 831, 64
Tinetti, G., Drossart, P., Eccleston, P., et al. 2016, Proc. SPIE, 9904, 99041X
Triaud, A. H. M. J., Dransfield, G., Kagetani, T., et al. 2023, MNRAS: Letters, 525, L98
van Saders, J. L., & Pinsonneault, M. H. 2012, ApJ, 751, 98
Virtanen, P., Gommers, R., Oliphant, T. E., et al. 2020, NatMe, 17, 261
Weiss, L. M., Marcy, G. W., Rowe, J. F., et al. 2013, ApJ, 768, 14
Welbanks, L., Bell, T. J., Beatty, T. G., et al. 2024, Natur, 630, 836
Welch, B. L. 1947, Biometrika, 34, 28
Wheeler, A. J., Casey, A. R., & Abruzzo, M. W. 2024, AJ, 167, 83
Wilson, J. C., Eikenberry, S. S., Henderson, C. P., et al. 2003, Proc. SPIE, 4841, 451
Wright, G. S., Rieke, G. H., Glasse, A., et al. 2023, PASP, 135, 048003
Wright, J. T., & Eastman, J. D. 2014, PASP, 126, 838
Yee, S. W., Petigura, E. A., & von Braun, K. 2017, ApJ, 836, 77
Zechmeister, M., & Kürster, M. 2009, A&A, 496, 577
Zechmeister, M., Reiners, A., Amado, P. J., et al. 2018, A&A, 609, A12